

Unravelling the role of inelastic tunneling into pristine and defected graphene

Mattias L. N. Palsgaard,¹ Nick P. Andersen,¹ and Mads Brandbyge¹

¹Center for Nanostructured Graphene, Dept. of Micro- and Nanotechnology,
Technical University of Denmark, Ørsted's Plads,
Bldg. 345E, DK-2800 Kongens Lyngby, Denmark

(Dated: October 31, 2021)

We present a first principles method for calculating the inelastic electron tunneling spectroscopy (IETS) on gated graphene. We reproduce experiments on pristine graphene and point out the importance of including several phonon modes to correctly estimate the local doping from IETS. We demonstrate how the IETS of typical imperfections in graphene can yield characteristic fingerprints revealing e.g. adsorbate species or local buckling. Our results show how care is needed when interpreting STM images of defects due to suppression of the elastic tunneling on graphene.

PACS numbers: 72.10.Di,68.37.Ef,63.22.Rc,63.20.dk

Imperfections such as lattice defects, edges, and impurity/dopant atoms can degrade the superb transport properties of graphene,^{1–4} or may, if controlled, lead to new functionality.⁵ Scanning Tunneling Microscopy/Spectroscopy (STM/STS) have been used extensively to obtain insights into the local electronic structure of graphene with atomic resolution.^{6–10} However, contrary to most STM/STS experiments where elastic tunneling plays the dominant role, for graphene the inelastic tunneling prevails. This was clearly demonstrated experimentally as a “giant” signal in the second derivative of the current w.r.t. voltage obtained in Inelastic Electron Tunneling Spectroscopy (IETS) performed on gated, pristine graphene with STM.^{6–8} The pronounced inelastic features are rooted in the electronic structure of graphene. The electrons have to enter the Dirac points corresponding to a finite in-plane momentum leading to weak elastic tunneling. The IETS signal of pristine graphene has been reproduced qualitatively by Wehling *et al.* considering the change in the wavefunction decay when displacing the carbon atoms along a selected frozen zone-boundary out-of-plane phonon.¹¹ In general, the important role of the inelastic process complicates the interpretation of STM results on graphene. Ideally STM images on graphene structures should be accompanied by local STS/IETS measurements, in order to distinguish between contributions from the inelastic and elastic channel. On the other hand, first principles calculations based on Density Functional Theory (DFT) often provide essential unbiased insights into STM/STS/IETS experiments to help the interpretation.

In this work we present a method for DFT calculations of the STS/IETS on gated graphene. We demonstrate its predictive power by reproducing from first principles the features of the experimental results for the giant inelastic conductance of gated pristine graphene.^{6–8} We then provide results for IETS signals of defected graphene systems determining the relative impact on the current of the various phonon modes. In particular we identify inelastic fingerprints of selected defects,

suggesting that IETS measurements can be a powerful tool in the characterization of imperfect graphene. Our analysis also illustrates how one should keep in mind the in-plane momentum conservation when performing STM on graphene. In particular we demonstrate how defects can locally lift the suppression of elastic tunneling. The resulting increased local conductance may be misinterpreted as a high local density of states (LDOS).

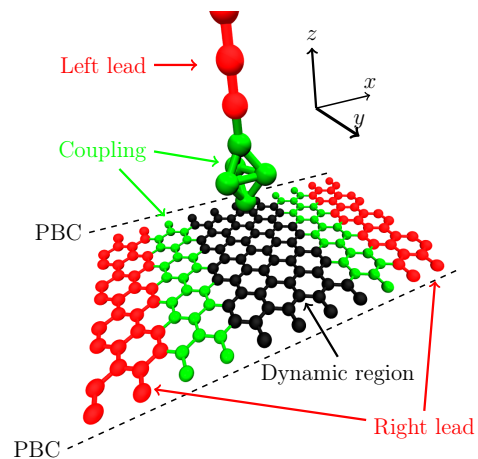


FIG. 1. (Color online) left: The system setup with semi-infinite leads (red), device region (green), dynamic region (black) and periodic boundary conditions along the dashed lines.

Method. The calculations are performed with DFT using the SIESTA/TranSIESTA^{12,13} code and the Inelastica package for inelastic transport.¹⁴ Our system shown in Fig. 1 is divided into device and “left”/“right” leads following the standard^{13,14} transport setup.¹⁵ We consider a suspended graphene sheet located 5 Å below the tip of a gold STM probe model. The “left” semi-infinite lead is attached to the probe, while the “right” semi-infinite leads are attached at *both* sides of the graphene sheet. We consider a voltage bias between “left” and “right” leads. The electron-phonon coupling (M^λ) is inherent to a cou-

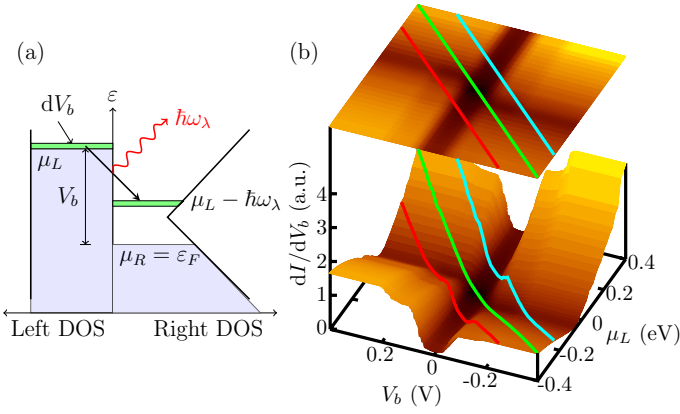


FIG. 2. (Color online) (a) Energy diagram showing the important (green) contributions of the left/right DOS when calculating the differential conductance for $V_b > \hbar\omega_\lambda$. (b) LOE differential conductance as a function of bias and tip (“left”) chemical potential. The lines ($\mu_L = eV_b + \varepsilon_F$) indicate the contours taken to include above threshold effects at a gate voltage (ε_F) of 0 eV (green) and ± 0.15 eV (blue/red).

pling region (green + black atoms in Fig. 1) of phonon modes (index λ) calculated in a dynamical region (black atoms). Floating orbitals are included between the STM tip and the graphene sample, to give a better description of the exponential decay of tunneling conductance.¹⁶

Following the Lowest Order Expansion (LOE),¹⁷ simplified and efficient expressions for the IETS signals can be derived under the assumption of weak electron-phonon coupling. The LOE expressions involve just the evaluation of the spectral density matrices for left/right moving states, $\mathbf{A}_{L/R}(\varepsilon)$, at the chemical potentials, $\varepsilon = \mu_L, \mu_R$, corresponding to the threshold voltage bias (V_b) for excitation of a given phonon (λ), $|\mu_L - \mu_R| = \hbar\omega_\lambda$. Thus the LOE expression does not *per se* reflect changes in the DOS above the phonon excitation threshold. However, in the context of STS on gated graphene, this is highly relevant since the behavior of the DOS leads to a distinct dip in the differential conductance at specific applied voltage, $V_b = V_D$,⁶ enabling a determination of the local chemical potential of graphene.

In order to encompass this important variation in the DOS above threshold we make the following observations (see also Fig. 2(a)). The expressions for the current which gives rise to inelastic signals have a form exemplified by the inelastic contribution to the current within LOE,

$$\begin{aligned}
 I_i \approx & \frac{e}{\hbar} \left(\coth \frac{\hbar\omega_\lambda}{2k_B T} - \coth \frac{\hbar\omega_\lambda - eV_b}{2k_B T} \right) \\
 & \times \int_{-\infty}^{\infty} d\varepsilon \text{Tr} \left[\mathbf{M}_\lambda \tilde{\mathbf{A}}_L(\varepsilon) \mathbf{M}_\lambda \mathbf{A}_R(\varepsilon - \hbar\omega_\lambda) \right] \\
 & \times \{ f_L(\varepsilon) - f_R(\varepsilon - \hbar\omega_\lambda) \}, \quad (1)
 \end{aligned}$$

where $\tilde{\mathbf{A}}_L$ is the time reversed left spectral function, and $f_{L/R}$ is the left/right occupation function. Here the coth-

terms yield the IETS-signal, namely a sharp step in the differential conductance, $\partial_{V_b} I_i$, for $V_b = \hbar\omega_\lambda$ at low temperature. Above threshold ($|V_b| > \hbar\omega_\lambda$) the step behavior is unimportant and we are left with the bias-behavior of the integral. For finite bias both the filling of states ($f_{L/R}$) as well as the states in the device, that is, the spectral functions, change with V_b . However, in this STM setup the device is strongly coupled to the right lead (graphene) and is very weakly coupled to the left lead (probe). Consequently the potential in the device is pinned to that of the right lead, which is the Fermi level $\mu_R = \varepsilon_F$ of the gated graphene lead. The DOS of the gold STM probe varies slowly w.r.t. energy. Thus if we define $\mu_L = \varepsilon_F + eV_b$ with the right chemical potential fixed at $\mu_R = \varepsilon_F$, the *only* important voltage dependent term is the Fermi-function, $f_L(\varepsilon) = n_F(\varepsilon - eV_b)$ inside the integral in Eq. (1) yielding an approximate δ -function in the differential conductance expression,

$$\partial_{V_b} I_i \approx \gamma_{i,\lambda} \partial_{V_b} \mathcal{I}^{\text{sym}}, \quad (2)$$

where

$$\gamma_{i,\lambda} = \text{Tr} \left[\mathbf{M}_\lambda \tilde{\mathbf{A}}_L(eV_b + \varepsilon_F) \mathbf{M}_\lambda \mathbf{A}_R(eV_b + \varepsilon_F - \hbar\omega_\lambda) \right], \quad (3)$$

and \mathcal{I}^{sym} is a universal function.¹⁷ We are therefore again left with evaluating the spectral functions at only two energies, $\varepsilon = eV_b + \varepsilon_F$ and $\varepsilon = eV_b + \varepsilon_F - \hbar\omega_\lambda$. Equation 2 is equivalent to the usual LOE expression but valid above threshold due to the constant tip-DOS. The same argument can be applied to the other terms in LOE.

In practice we calculate the LOE differential conductance for a range of μ_L , see Fig. 2(b), and can obtain the differential conductance by following the contour along the $\mu_L = V_b$ direction (green line), and projecting it onto the $dI/dV_b, V_b$ plane. Gating the graphene sheet corresponds to shifting the Fermi level by a constant over all bias voltages, and can be obtained from Fig. 2(b) by a translation of the contour along the chemical potential axis.

Results — pristine graphene. Calculated STS spectra on pristine graphene for a number of different Fermi levels are shown in Fig. 3(a). The gap feature around $V_b = 0$ of width 0.13 V is reproduced in detail and the dip at V_D , caused by inelastic tunneling into the charge neutrality point of graphene, appears outside the gap as seen in experiments.^{6–8} As the gate is applied, V_D moves across the spectrum changing polarity while the position and width of the gap feature is stable. The inset shows how significant the difference in results are when ignoring/including above threshold terms. It also shows how the usual LOE calculation works well below threshold and captures the inelastic steps.

Most major steps in differential conductance come from acoustic out-of-plane phonons at energies just below 67 meV.¹⁸ In particular the mode shown in Fig. 3(b) gives a

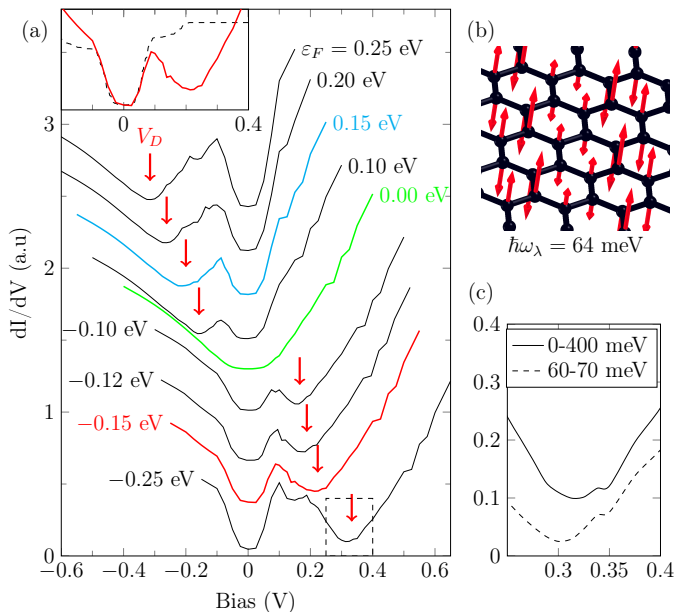


FIG. 3. (Color online)(a) Calculated STS spectra of pristine graphene at different Fermi levels. Colors represent the lines in Fig. 2(b). Inset: Comparison between STS spectra, at $\varepsilon_F = -0.15$ eV including/ignoring (red/black) DOS effects above threshold bias. (b) Out-of-plane acoustic graphene phonon. (c) Close-up of the dip at V_D for $\varepsilon_F = -0.25$ eV, including phonons in different energy ranges.

large contribution. However we find that acoustic out-of-plane graphene phonons with energies as low as 42 meV give considerable contributions as well. We also find important inelastic signals from optical graphene phonons at energies above 67 meV. The additional features away from 67 meV make up about half the signal, and have not been included in previous studies.¹¹ If we restrict our calculations to phonons in the 60–70 meV range, we obtain a 15 mV change in (V_D) , see Fig. 3(c), and changes in both the width and height of the inelastic gap. The change in V_D is caused mostly by the experimentally observed⁸ inelastic signal near 150 mV, coming from the optical in-plane modes, and occurs for $|V_D| > 150$ mV. In STS experiments V_D is used to extract the energy position of the charge neutrality point from $E_D = e|V_D| - \hbar\omega_0$ where $\hbar\omega_0 = 63$ meV is half the width of the gap feature which corresponds to the energy of an acoustic out-of-plane graphene phonon.^{6,7} The change in V_D could explain why all points with $|E_D| < 100$ meV in the E_D vs gate voltage plot of Ref. 7 fall below the fitted line. Local charge-carrier density (n) of graphene is also extracted from V_D in STS experiments.^{7,9,10} Mistaking $E_D = 100$ meV for $E_D = 115$ meV results in a 32% error in n . To capture these experimental details one must include several phonons, and account for their impact in an *ab initio* manner.

Encouraged by the agreement for pristine graphene we next predict the inelastic signals from various defects to

shed light on what information can be obtained from STM-IETS.

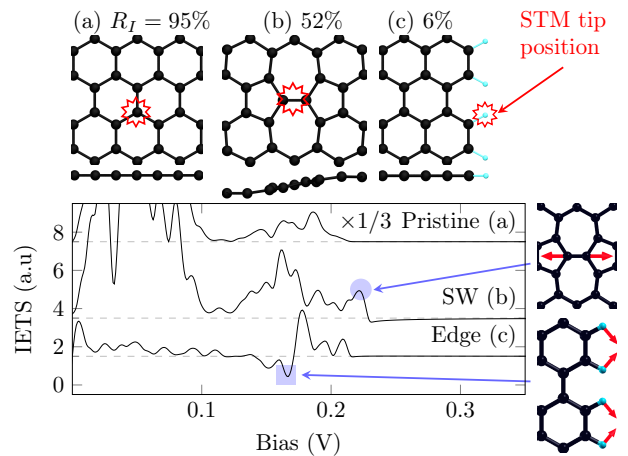


FIG. 4. IETS as a function of bias for pristine graphene, a Stone-Wales defect, and a hydrogen passivated armchair edge (geometries shown above plot). The blue marker indicate characteristic signals. The fraction of differential conductance coming from the inelastic channel (R_I) is shown above the geometries.

Results — Structurally defected graphene. In Fig. 4 we show the calculated IETS spectra from an on-top position in pristine graphene (a), directly above a Stone-Wales defect (SW) (b), and above a passivated armchair edge (c). The result shown for pristine graphene is the same at hollow sites and bridge sites. We find that the gap feature and low voltage IETS above a SW is very similar to that of pristine graphene. The gap has also been observed experimentally for regions with heptagon-pentagon defects.¹⁹ However, a characteristic signal can be seen at $V_b = 223$ mV bias, above any of the pristine graphene phonon bands which can be traced to the high frequency stretch mode localized at the twisted C-C bond shown in Fig. 4.

Ignoring the out-of-plane buckling introduced to the graphene sheet near a SW, and calculating the IETS for a flat SW system, leads to a 5 mV blue-shift of the signal from the twisted C-C bond as previously proposed.²⁰ We also see strong signals at low bias. These signals are caused by low-frequency sine-like out-of-plane modes. These modes couple strongly to the current because they break the mirror symmetry across the twisted C-C bond. In the buckled system, this symmetry is inherently broken, leading to an increase in elastic tunneling. Measuring strong low bias inelastic signals and a 228 mV signal above a SW therefore indicates that it is in a metastable flat configuration, whereas increased elastic transmission and a 223 mV signal is a sign of local buckling. Above a passivated armchair edge a dip in IETS is seen at $V_b = 168$ mV caused by a

collective transverse mode of the Hydrogen atoms shown in Fig. 4. Changing the mass of the passivating agent to that of Fluor, we observe a corresponding change in the position of the inelastic signals. This indicates that IETS can be used to obtain knowledge of graphene edge passivation.

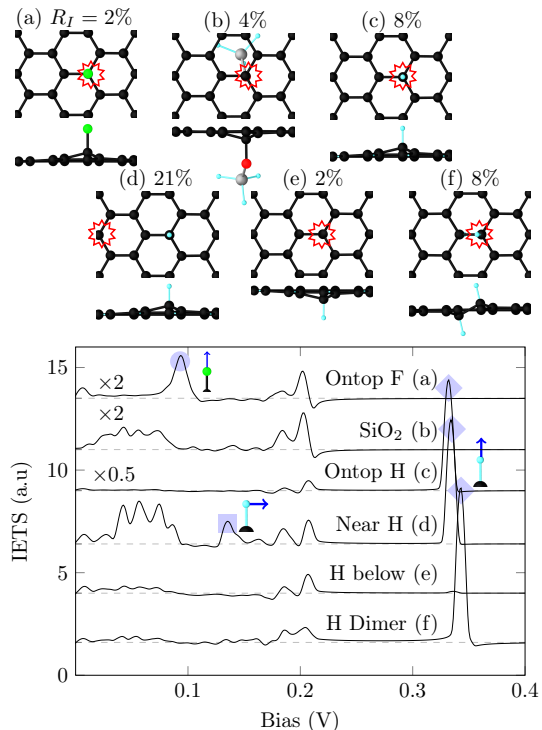


FIG. 5. IETS as a function of bias voltage, for various adsorbates on graphene (geometries shown above plot). Fingerprints for each adsorbate is marked and the phonon shown. The fraction of differential conductance coming from the inelastic channel (R_I) is shown above the geometries.

Results — Adsorbates on graphene. In Fig. 5 we show IETS spectra from a range of different covalently bonded impurities (Fluor, Hydrogen) and a model of strong interaction to a SiO_2 substrate. In Fig. 5(a) a clear inelastic signal from the longitudinal mode of a Fluor adsorbate is seen at 95 mV. Above a Hydrogen adsorbate, we see a strong inelastic peak at 332 mV caused by the stretch mode of the C-H bond (see Fig. 5(c)). This signal serves as a fingerprint for a Hydrogen impurity above the graphene sheet as opposed to below where the signal disappears as can be seen in Fig. 5(e). The corresponding STS spectra show a strong zero-energy peak²¹, this behavior is however expected for all covalently bonded impurities,²² above or below the sheet, and can therefore not be used as a fingerprint. The STS spectra on the hydrogenated system with the probe above a Carbon atom 4.25 Å laterally away from the impurity in Fig. 5(d), shows additional signals. The graphene out-of-plane phonon signals reappear and a

signal is also seen at 134 mV caused by a transverse mode of the C-H bond. Above a graphane-like hydrogen dimer Fig. 5(f) the signal caused by the C-H bond stretch mode is seen, however here it is caused by two degenerate modes and blue-shifted by 11–16 mV indicating a lower energy configuration.

Common for all the imperfect systems is that the gap seen in pristine graphene is quenched as indicated by the severe reduction of the inelastic conductance ratio (R_I) in Fig. 4 and 5. Out-of-plane corrugations in the graphene sheet can lift the suppression of elastic tunneling if they are on the same length scale as the graphene lattice constant.¹¹ Our results indicate that defects can also lift the suppression locally. This is because the selection rules causing the suppression in pristine graphene is a result of the translational symmetry of the crystal lattice. When this symmetry is broken the suppression is lifted and the elastic tunneling dominates. The expected order of magnitude change in tunneling conductance should lead to bright spots in STM topographies. In the case of granular CVD graphene protruding grain boundaries are often attributed to localized electronic states.¹⁹ Our results here point out that one may expect increased tunneling near disordered areas of graphene, even if no localized electronic states are present and the area is completely flat. As seen in Fig. 5(b)(e) this is also the case for strong interaction with a SiO_2 substrate or adsorbates sitting below the graphene sheet, which should therefore be visible as protruding from the graphene sheet.

In summary, we have presented a first principles method and used it for calculations of IETS and STS spectra of pristine and defected graphene. We showed how measured STS spectra on pristine gated graphene can be reproduced in detail as a function of gating. The inclusion of several phonons had a strong impact on all aspects of the STS spectrum of pristine graphene. In particular we found that including optical in-plane phonons changed the V_D value for certain gate voltages. This is of importance for studies where IETS is used to probe the local doping of graphene^{7,9,10} where it may lead to a significant overestimation of the local charge inhomogeneity. We predicted the IETS of typical imperfections in graphene, and demonstrated how these can yield characteristic fingerprints revealing e.g. adsorbate species or local buckling. Additional elastic contributions above defects should make them protrude in STM regardless of actual geometric or electronic structure and care is needed when interpreting STM images.

We gratefully acknowledge discussions with Thomas Frederiksen, Aran Garcia-Lekue and Rasmus Bjerregaard Christensen.

-
- [1] A. Geim and K. S. Novoselov, *Nat. mat.* **6**(3), 183 (2007).
- [2] A. H. C. Neto, F. Guinea, N. M. R. Peres, K. S. Novoselov, and A. K. Geim, *Reviews of modern physics* **81**(1), 109 (2009).
- [3] K. S. Novoselov, A. K. Geim, S. V. Morozov, D. Jiang, Y. Zhang, S. V. Dubonos, I. V. Grigorieva, and A. A. Firsov, *Science* **306**, 666 (2004).
- [4] A. C. Ferrari, J. C. Meyer, V. Scardaci, C. Casiraghi, M. Lazzeri, F. Mauri, S. Piscanec, D. Jiang, K. S. Novoselov, S. Roth, and A. K. Geim, *Phys. Rev. Lett.* **97**, 187401 (2006).
- [5] J. Pedersen, T. Gunst, T. Markussen, and T. Pedersen, *Phys. Rev. B* **86** (2012).
- [6] Y. Zhang, V. W. Brar, F. Wang, C. Girit, Y. Yayon, M. Panlasigui, A. Zettl, and M. Crommie, *Nat. Phys.* **4**, 627 (2008).
- [7] R. Decker, Y. Wang, V. W. Brar, W. Regan, H. Z. Tsai, Q. Wu, W. Gannett, A. Zettl, and M. F. Crommie, *Nano Letters* **11** (2011).
- [8] V. W. Brar, S. Wickenburg, M. Panlasigui, C.-H. Park, T. O. Wehling, Y. Zhang, R. Decker, i. m. c. b. u. Girit, A. V. Balatsky, S. G. Louie, A. Zettl, and M. F. Crommie, *Phys. Rev. Lett.* **104**, 036805 (2010).
- [9] P. Cao, J. O. Varghese, K. Xu, and J. R. Heath, *Nano Letters* **12**, 1459 (2012).
- [10] S. J. Goncher, L. Zhao, A. N. Pasupathy, and G. W. Flynn, *Nano Letters* **13**, 1386 (2013).
- [11] T. O. Wehling, I. Grigorenko, A. I. Lichtenstein, and A. V. Balatsky, *Phys. Rev. Lett.* **101**, 216803 (2008).
- [12] J. M. Soler, E. Artacho, J. D. Gale, A. García, J. Junquera, P. Ordejón, and D. Sánchez-Portal, *J. Phys.: Condens. Matter* **14**, 2745 (2002).
- [13] M. Brandbyge, J. L. Mozos, P. Ordejón, J. Taylor, and K. Stokbro, *Phys. Rev. B* **65**, 165401 (2002).
- [14] T. Frederiksen, M. Paulsson, M. Brandbyge, and A. P. Jauho, *Phys. Rev. B* **75**, 205413 (2007).
- [15] We use a split DZP basis set, a mesh cutoff of 200 Ry, a Monkhorst-Pack k -point mesh of $1 \times 1 \times 1$ and the LDA xc-functional²³ to calculate the electronic structure. Supercell dimension (k_y -points) of $27 \text{Å} \times 12.8 \text{Å}(101)/34.5 \text{Å} \times 25.5 \text{Å}(\Gamma)/49.3 \text{Å} \times 12.8 \text{Å}(\Gamma)/27 \text{Å} \times 17 \text{Å}(\Gamma)$ is used for inelastic transport for the pristine/SW/edge/adsorbate configuration.
- [16] A. Garcia-Lekue and L. W. Wang, *Phys. Rev. B* **82**, 035410 (2010).
- [17] J. T. Lü, R. B. Christensen, G. Foti, T. Frederiksen, T. Gunst, and M. Brandbyge, *Phys. Rev. B* (2014).
- [18] M. Mohr, J. Maultzsch, E. Dobardzic, S. Reich, I. Milocevic, M. Damnjanovic, A. Bosak, M. Krisch, and C. Thomsen, *Phys. Rev. B* **76**, 035439 (2007).
- [19] L. Zhao, M. Levendorf, S. Goncher, T. Schiros, L. Paova, A. Zabet-Khosousi, K. T. Rim, C. Gutierrez, D. Nordlund, C. Jaye, M. Hybertsen, D. Reichman, G. W. Flynn, J. Park, and A. N. Pasupathy, *Nano Letters* **13**, 4659 (2013).
- [20] J. Ma, D. Alfe, A. Michaelides, and E. Wang, *Phys. Rev. B* **80**, 033407 (2009).
- [21] M. Scheffler, D. Haberer, L. Petaccia, M. Farjam, R. Schlegel, D. Baumann, T. Hänke, A. Gruneis, M. Knupfer, C. Hess, and B. Buchner, *ACS Nano* **6**, 10590 (2012).
- [22] T. O. Wehling, M. I. Katsnelson, and A. I. Lichtenstein, *Phys. Rev. B* **80**, 085428 (2009).
- [23] J. P. Perdew and A. Zunger, *Phys. Rev. B* **23**, 5048 (1981).